applied sciences

MDPI

Article

Fractal Behavior of Size Distribution and Specific Surface Area of Blasting Fragments

Ruize Li [1,2,3], Peng Zhu [1,3], Shuyi Li [3,*], Cong Ding [1,3], Wenbo Lu [4] and Yijia Liu [1,3,*]

[1] Zhejiang Huadong Engineering Construction Management Co., Ltd., Hangzhou 310014, China; li_rz5@hdec.com (R.L.); zhu_p@hdec.com (P.Z.); ding_c5@hdec.com (C.D.)
[2] Key Laboratory of Geotechnical Mechanics and Engineering of the Ministry of Water Resources, Yangtze River Scientific Research Institute, Wuhan 430010, China
[3] Zhejiang Engineering Research Center of Green Mine Technology and Intelligent Equipment, Hangzhou 310014, China
[4] State Key Laboratory of Water Resources Engineering and Management, Wuhan University, Wuhan 430072, China; wblu@whu.edu.cn
* Correspondence: li_sy@hdec.com (S.L.); liu_yj7@hdec.com (Y.L.)

Abstract: The shape characteristics of blasting fragments are important for analyzing the blasting fragmentation mechanism and evaluating the fragmentation energy efficiency. In this study, through field blasting experiments and morphological parameter measurements, fractal theory was employed to reveal the fractal characteristics of rock blasting fragmentation. Using the fragmentation fractal dimension, the probability of rock blasting fragmentation was analyzed, and a predictive formula for the specific surface area (SSA) of blasting fragments was established. For fragments, the fractal dimensions of the particle size distribution calculated using different characteristic sizes were less than 2.0. When the fragment size distribution had dual fractal characteristics, significant differences were observed in the scale-free interval and fragmentation fractal dimension. Within the large scale-free interval, the fragmentation fractal dimension was mostly greater than 2.3, whereas within the small scale-free interval, it tended to be less than 2.0. The rock fragmentation process typically consisted of two or three breakage levels, with a similarity ratio of 0.5 and an average fragmentation probability ranging from 0.44 to 0.71. The predicted SSA of the blasting fragments closely matched the measured values. The findings provide valuable insights into the mechanism of rock blasting fragmentation and the calculation of fragmentation energy consumption.

Keywords: drilling and blasting; bench blasting; blasting fragments; fractal dimension; fragmentation size distribution

check for updates

Citation: Li, R.; Zhu, P.; Li, S.; Ding, C.; Lu, W.; Liu, Y. Fractal Behavior of Size Distribution and Specific Surface Area of Blasting Fragments. *Appl. Sci.* **2023**, *13*, 11832. https://doi.org/10.3390/app132111832

Received: 28 September 2023
Revised: 24 October 2023
Accepted: 27 October 2023
Published: 29 October 2023

Copyright: © 2023 by the authors. Licensee MDPI, Basel, Switzerland. This article is an open access article distributed under the terms and conditions of the Creative Commons Attribution (CC BY) license (https://creativecommons.org/licenses/by/4.0/).

1. Introduction

Drilling and blasting are the initial processes of the mine-to-milling sequence, and the properties of blasting fragments significantly affect the overall production costs of mine-to-milling processes [1–3]. Studies have indicated that the particle size distribution, shape, and specific surface area (SSA) are fundamental attributes of blasting fragments, which affect the energy utilization efficiency of downstream crushing equipment [4–6]. Therefore, investigating the fundamental attributes of blasting fragments has theoretical significance for clarifying the mechanism of rock blasting fragmentation and optimizing the energy efficiency throughout the mine-to-milling process.

Blasting fragments are typical irregular particles with fragments ranging in size from the order of microns to meters. Therefore, evaluating their basic attributes is difficult [3,7]. Currently, particle size measurement techniques are well-established, leading to various research outcomes regarding particle size distribution measurement and fragment size distribution characteristics. The sieve test is the simplest method of measuring particle size distributions [8] but involves substantial work and high testing costs [9]. Thus, various approaches, such as distribution function methods, artificial intelligence algorithms,

and digital image processing techniques, are utilized to obtain fragment size distribution curves rapidly. The models most often used in distribution function methods are the Kuz–Ram model, Kuznetsov–Cunningham–Ouchterlony model, xP-frag model, and fragmentation–energy fan model [7]. However, owing to the variable nature of rock mass, the parameter selection for distribution models varies among researchers, leading to significant discrepancies in the calculation results among different models. With the development of new technologies such as machine learning and big data, scholars have used various intelligent algorithms, e.g., particle swarm optimization and bacterial foraging optimization, to establish multiple fragment size distribution prediction models by training and optimizing data from blasting experiments [10,11]. However, this approach requires a large amount of data and strong programming skills. Since the 1980s, image processing techniques have been used for blasting fragmentation distribution measurement. With advancements in stereophotography, machine vision, and three-dimensional (3D) laser scanning technologies, image processing has become the preferred tool for measuring fragment size distribution in most engineering blasting scenarios. Software programs such as WipFrag, Split, and Gold Size are examples of image processing tools that are widely used for analyzing fragment size distributions [12]. Onederra et al. [13], Chen et al. [14], and Campbell et al. [15] employed 3D laser scanning and image processing techniques to obtain the in situ block size distribution of rock mass.

Early methods of studying particle shape characteristics involved indirect tests that quantified particle shape through physical and mechanical parameters such as porosity [16]. However, indirect experimental results represent overall particle shape characteristics and cannot describe the shape features of individual particles [17,18]. Presently, visualization, manual caliper measurement, and digital image processing are commonly used to assess particle shape characteristics [19]. Visualization and caliper measurement are simple and inexpensive methods of evaluating the form and angularity of a large quantity of particles or particles with large diameters [20]; however, the results are subjective. Therefore, digital image processing methods are more widely used. For instance, Blott et al. [21] and Tunwal et al. [22] employed digital image processing techniques to study the surface texture of sediment particles, such as roundness and angularity. Zhu et al. [23] utilized charge-coupled device cameras and 3D laser scanners to study the angularity of coarse aggregates. As mentioned previously, the existing methods can only characterize the shape features of particles within a certain particle size range [24], whereas the particle size and shape of blasting fragments vary widely [3,7], posing challenges to the characterization of their shape properties [25,26].

Fractals allow the quantification of seemingly chaotic and randomly distributed phenomena and behaviors [27]. Research indicates that the defects, shapes, strength, deformation, and energy consumption of rock and soil materials all exhibit statistical self-similarity at certain scales, i.e., fractal characteristics [28]. Fractals have become important tools in rock mechanics research. The fractal dimension is the primary parameter for describing fractals [28] and has been widely used in various applications, such as mineral particle morphology analysis [29,30], rock damage assessment [31], and fragmentation evaluation [32]. During the process of rock fragmentation, the fractal dimension can continuously change at different resolutions (different lengths of the measuring stick), allowing the target object to exhibit dual or multifractal characteristics [27]. Extensive studies on fragmentation phenomena have indicated that the fractal dimension of rock fragmentation typically falls between 2.0 and 3.0 [28]. In previous research, the fractal dimension was often fitted according to the fragment size distribution to assess the fragmentation quantitatively [33,34].

In summary, as blasting fragments are typical irregular particles, most previous studies focused on characterizing the shape features of rock particles within a small particle size range. Limited research exists on the shape and fractal characteristics of blasting fragments across the entire particle size range. Furthermore, SSA is a useful indicator for calculating rock fragmentation energy, as it comprehensively reflects particle size and shape characteristics [3]. Neglecting the shape properties of blasting fragments would inevitably

reduce the accuracy of SSA calculations along with the accuracy of evaluating the explosive energy utilization efficiency [35–37]. Thus, fractal theory must be used to study the shape characteristics of blasting fragments across the entire particle size range.

In this study, seventeen field blasting tests at four quarries and indoor measurements of shape parameters of randomly collected blasting fragments were performed. Image processing techniques were employed to obtain blasting fragmentation distribution for each test. Using fractal theory, the fractal dimensions of the particle size distribution and fragmentation were calculated, revealing the multifractal characteristics of rock blasting fragmentation and clarifying the probability of rock blasting fragmentation. Moreover, a predictive formula for the SSAs of blasting fragments was established using the fragmentation fractal dimension.

2. Material and Methods

2.1. Field Blasting Experiments

To investigate the fractal characteristics of blasting fragments, a total of seventeen deep-hole bench blasting experiments were conducted at four quarries. The test locations in each quarry are depicted in Figure 1, and the blasting parameters for each experiment are presented in Table 1. The primary physical and mechanical parameters of the rock mass within the experiment areas are presented in Table 2.

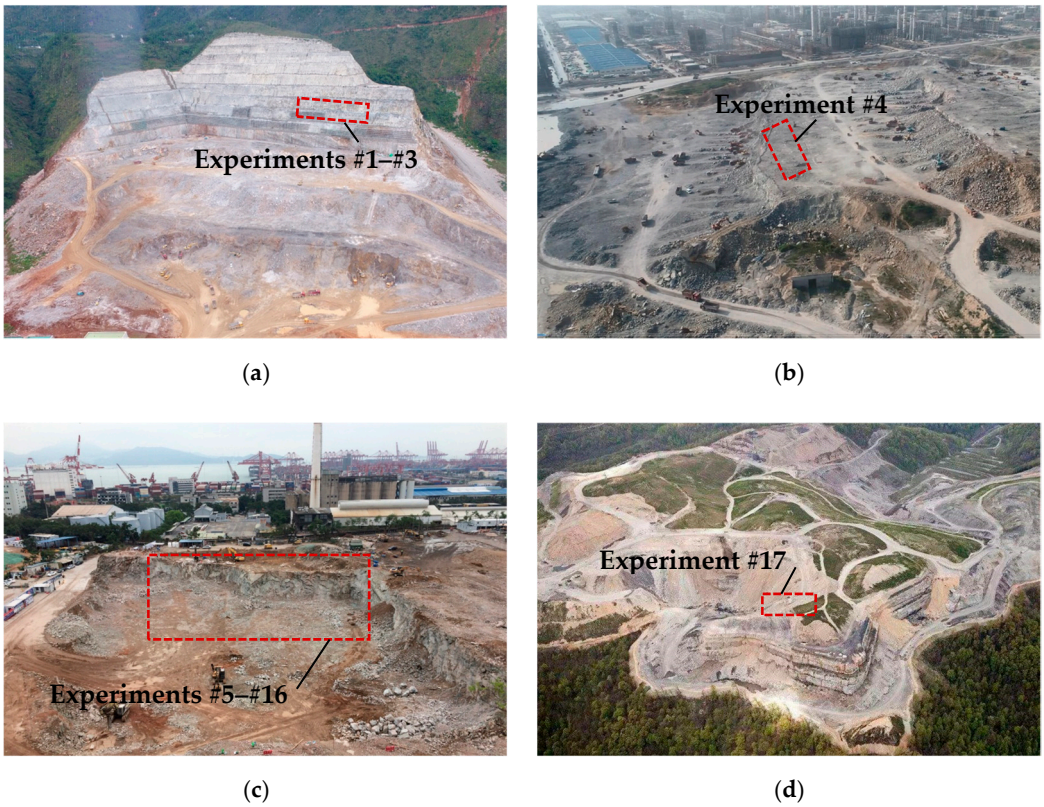


Figure 1. Locations of the bench blasting experiments: (**a**) quarry Q_1; (**b**) quarry Q_2; (**c**) quarry Q_3; (**d**) quarry Q_4.

Among the twelve blasting experiments conducted in quarry Q_3, experiments #12–#16 involved conventional bench blasting experiments, experiments #5–#10 involved blasting with shock-reflection devices, and experiment #11 involved water-decked blasting. The typical charging construction for blasting with shock-reflection devices and water-decked blasting experiments is illustrated in Figure 2. Experiment #17 employed a mixture of porous granular ammonium nitrate explosive and featured a continuous charging construction.

Table 1. Blasting experiment parameters for each quarry.

Quarry Code	Code	Bench Height (m)	Hole Diameter (mm)	Explosive Diameter (mm)	Hole Depth (m)	Subdrill (m)	Specific Charge (kg/m^3)	Hole Spacing (m)	Row Spacing (m)	Stemming Length (m)
Q_1	#1	15	115	70	14.8–17.0	1.0	0.38	6.0	4.0	4.5
	#2	15	115	70	16.2–18.0	1.0	0.35	5.0	4.0	4.5
	#3	15	115	70	15.5–18.4	1.0	0.35	6.0	4.0	5.0
Q_2	#4	12	115	90/70	13.0–15.0	1.0	0.32	4.5	4.5	4.5–5.0
Q_3	#5	12	115	90	10.6–13.4	0.8–1.0	0.35	4.0	3.5	3.5–4.0
	#6	12	115	90	10.6–13.4	0.8–1.0	0.35	4.0	3.5	3.5–4.0
	#7	12	115	90	10.6–13.4	0.8–1.0	0.35	4.0	4.0	3.5–4.0
	#8	8	115	60	8.0–9.4	0.4–0.6	0.36	2.3	2.0	2.0–2.5
	#9	8	115	60	5.9–8.0	0.4–0.6	0.36	2.0	2.0	1.0–2.5
	#10	8	115	60	8.0–9.4	0.4–0.6	0.36	2.0	1.8	2.0–2.5
	#11	12	115	90	11.0–13.4	0.8–1.0	0.35	4.0	3.5	3.5–4.0
	#12	12	115	90	10.6–13.4	0.8–1.0	0.35	4.0	4.0	3.5–4.0
	#13	12	115	90	10.6–13.4	0.8–1.0	0.35	4.0	4.0	3.5–4.0
	#14	8	115	60	8.0–9.4	0.4–0.6	0.36	2.3	2.0	2.0–2.5
	#15	8	115	60	8.0–9.4	0.4–0.6	0.36	2.0	2.0	1.0–2.5
	#16	8	115	60	8.0–9.4	0.4–0.6	0.36	2.0	1.8	2.0–2.5
Q_4	#17	15	160	160	16.5	1.5	0.36	7.5	5.0	3.5

Table 2. Key physical and mechanical properties of the rock mass in the experimental area.

Experiment Area	Rock Type	Natural Density (g/cm^3)	Young's Modulus (GPa)	Poisson's Ratio	Unconfined Uniaxial Compressive Strength (MPa)
Quarry Q_1	Mildly weathered limestone	2.69–2.71	45–55	0.23	113–140
Quarry Q_2	Mildly weathered tuff	2.60	80	0.21	140–190
Quarry Q_3	Mild to moderately weathered granite	2.61	50	0.22	45–75
Quarry Q_4	Mildly weathered limestone	2.68–2.70	16	0.22	31.4–94.6

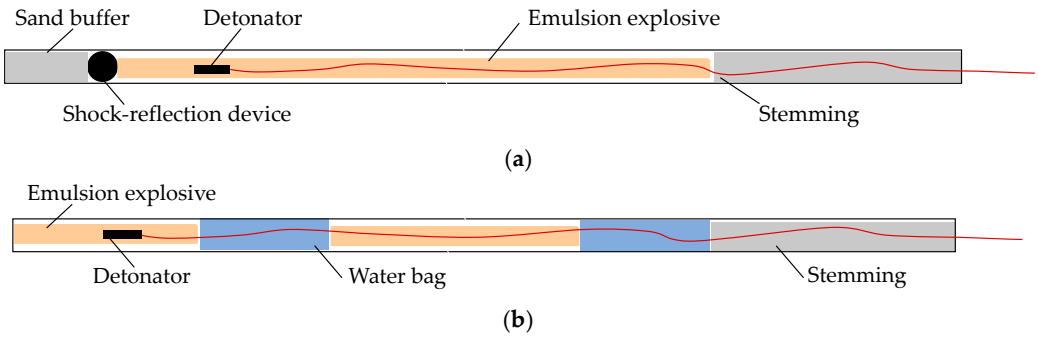


Figure 2. Typical charging construction for the field blasting experiments: (**a**) blasting with shock-reflection devices; (**b**) water-decked blasting.

2.2. Blasting Fragmentation Distribution Curve Detection Experiments

During open-pit mining, the muck pile volume typically reaches thousands of cubic meters, with the maximum particle size exceeding 1000 mm [7]. In this context, conducting sieve tests for measuring blasting fragmentation distribution curves is expensive and requires substantial sampling effort and long test durations; additionally, it may interfere with other production processes [9,38]. Therefore, in this study, image processing techniques were employed to measure the blasting fragmentation distribution curves for each experiment.

To ensure accuracy, eighteen to twenty-five images of the blasting fragments were collected from cross-sections formed on the surface of the muck pile or during the shoveling

and loading processes [39]. The static image capture method was utilized during the experiments, and ten to twenty representative images were selected for processing. It was ensured that each image contained at least four hundred blasting fragments. Representative images with their image processing outcomes are shown in Figure 3, and the blasting fragmentation distribution curves for each experiment are presented in Figure 4.

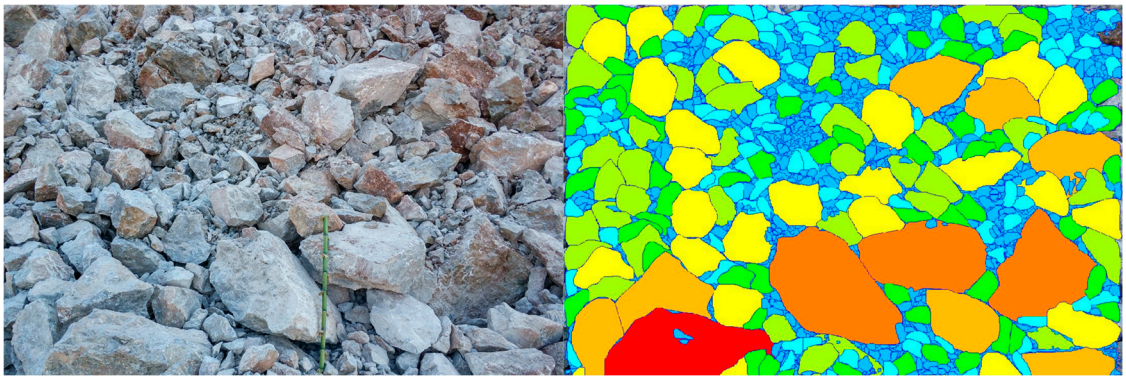


Figure 3. Typical blasting fragments and their segmented outlines in quarry Q_1.

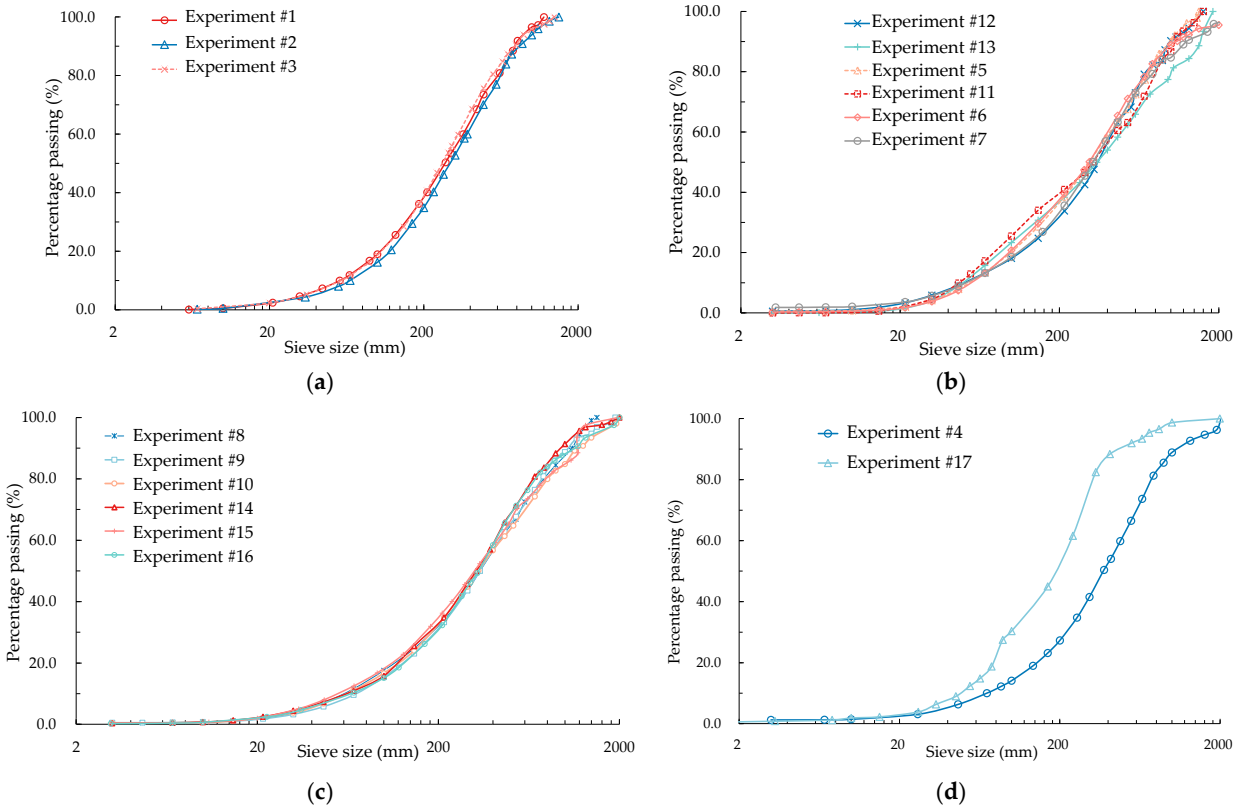


Figure 4. Blasting fragmentation distribution curves for each experiment: (**a**) experiments #1–#3; (**b**) experiments #5–#7 and #11–#13; (**c**) experiments #8–#10 and #14–#16; (**d**) experiments #4 and #17.

2.3. Shape Characteristics and SSA Measurement Experiments

After the blasting experiments, a certain number of blasting fragments were randomly collected from muck piles for indoor shape parameter measurement experiments. The top, middle, and bottom of the muck piles each had five uniformly distributed sampling points. Approximately equal quantities of fifteen fragment samples were extracted from each subsampling point, forming a bulk sample group. The distribution of sampling points

in the upper, middle, and lower layers of the muck pile, as well as the subsampling points within the sampling points, are illustrated in Figure 5.

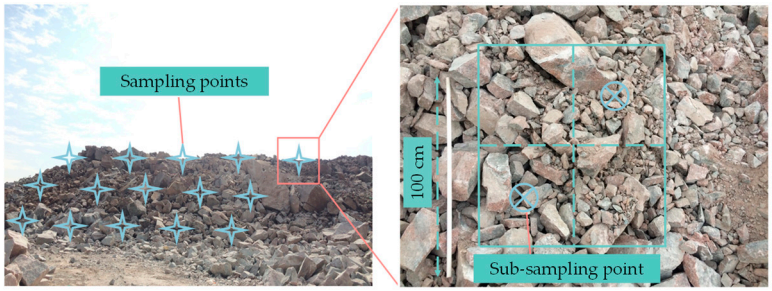


Figure 5. Arrangement of blasting fragment sampling points and subsampling points in quarry Q_3.

In this study, 322, 209, 1878, and 285 blasting fragments were randomly collected from quarries Q_1, Q_2, Q_3, and Q_4, respectively. Subsequently, image processing techniques were employed to calculate the particle size and shape parameters of each blasting fragment. The SSA was computed using an equivalent ellipsoid model, and the calculation process and results can be found in previous works [3,40]. The calculation formula was as follows:

$$\mathrm{SSA} = \frac{S}{\rho V} = \frac{\alpha_1 4\pi {r_1}^2}{\rho \frac{4}{3}\pi {r_1}^3} = \frac{3\alpha_1}{\rho r_1}, \tag{1}$$

where α_1 is the equivalent ellipsoid correction coefficient, and r_1 represents the equivalent radius of the ellipsoid (cm), which is given as

$$r_1 = \left(a^2 c\right)^{\frac{1}{3}}. \tag{2}$$

Here, a and c represent the long and short axes, respectively, of the equivalent ellipsoid. Assuming that the proportions of blasted fragments with $a > c$ and $a < c$ were equal, α_1 was calculated with a weight of 0.5.

For $a > c$, α_1 was calculated as follows:

$$\alpha_1 = \frac{2\pi a + \frac{2\pi a c^2}{\sqrt{a^2 - c^2}} \cdot \ln\left(\frac{a + \sqrt{a^2 - c^2}}{c}\right)}{\frac{4\pi a^2 c}{3}} \cdot \frac{r_1}{3}. \tag{3}$$

For $a < c$, α_1 was calculated as follows:

$$\alpha_1 = \frac{2\pi a c^2 \sqrt{\frac{1}{c^2 - a^2}} \cdot \arcsin\frac{\sqrt{c^2 - a^2}}{c} + 2\pi a^2}{\frac{4\pi a^2 c}{3}} \cdot \frac{r_1}{3}. \tag{4}$$

3. Theory and Calculation Results

3.1. Theory for Fractal Dimensions of Particle Size Distribution

The fractal features of rock particles are predominantly quantified using two methods: particle size–frequency and mass–frequency [28].

Considering particle size–frequency,

$$N = N_0 (d_i / d_{\max})^{-D}, \tag{5}$$

where N represents the number of rock particles with characteristic sizes greater than or equal to d_i, N_0 represents the number of rock particles with the largest characteristic size d_{max}, and D represents the fractal dimension of the particle size distribution.

When calculating the fractal dimensions of the particle size distribution using Equation (5), a uniform particle shape and density must be assumed. These assump-

tions often lead to significant errors. Tyler et al. postulated a constant density for particles of varying sizes and, by employing strict self-similarity, derived a 3D model for the fractal distribution of rock particles based on the size–cumulative mass relationship [41].

Under a constant density, the mass of rock particles with diameters exceeding a characteristic diameter d_i is expressed as

$$M(d > d_i) = \rho C_V \left[1 - \left(\frac{d_i}{\lambda_V}\right)^{3-D_F}\right], \tag{6}$$

where D_F represents the fractal dimension of rock fragmentation; C_V and λ_V are constants related to the rock particle size and shape, respectively; and ρ represents the density of rock particles.

When d_i is set to zero, the total mass of rock particles in the muck pile, as calculated using Equation (6), is

$$M_T = \rho C_V. \tag{7}$$

Rock particles with diameters exceeding the maximum diameter d_{max} in the muck pile have zero mass. Substituting this into Equation (6) yields

$$\lambda_V = d_{\max}. \tag{8}$$

According to Equations (5)–(8), it follows that

$$\frac{M(d < d_i)}{M_T} = 1 - \frac{M(d > d_i)}{M_T} = \left(\frac{d_i}{d_{\max}}\right)^{3-D_F}. \tag{9}$$

Taking the logarithm of both sides of Equation (9) yields

$$\log\left[\frac{M(d < d_i)}{M_T}\right] = (3 - D_F)\log\left(\frac{d_i}{d_{\max}}\right). \tag{10}$$

3.2. Calculation of Fractal Dimensions of Particle Size Distribution

According to the image processing results for the shape parameters presented in Section 2.3, the power-law fractal distribution curves of the minimum enclosing cubic dimensions (L, I, S) of the blasting fragments were obtained for each experiment, as shown in Figure 6.

For small particles, size measurement through image processing is relatively inaccurate, and the number of large particles in the muck piles is limited. Consequently, data deviations are observed at both ends in Figure 6, which can adversely affect the fitting of the power-law fractal distribution curve. Therefore, data with particle sizes greater than 5 mm but less than 900 mm were employed for fitting in this study. The results are presented in Table 3.

As shown in Figure 6 and Table 3, the coefficient of determination (R^2) for fitting the power-law fractal distribution of blasting fragments via the particle size–frequency method for all four quarries was greater than 0.94, indicating a good fitting effect. The fractal dimensions of the particle size distribution obtained through three characteristic dimensions for each of the four quarries were all less than 2. Additionally, significant differences existed in the fractal dimensions of the particle size distribution obtained using different characteristic dimensions, indicating that the characteristic dimensions significantly affected the fractal dimensions of the particle size distribution. This result is consistent with the findings of Li et al. [42] concerning the fractal characteristics of granite rock fragments resulting from blasting experiments. Furthermore, quarry Q_4 exhibited a significantly larger fractal dimension of the size distribution for limestone blasting fragments. We attribute this to the use of mixed-porous granular ammonium nitrate explosives in test #17. In this case, the coupled explosive charging construction enhanced the fragmentation under the influence of blast loads.

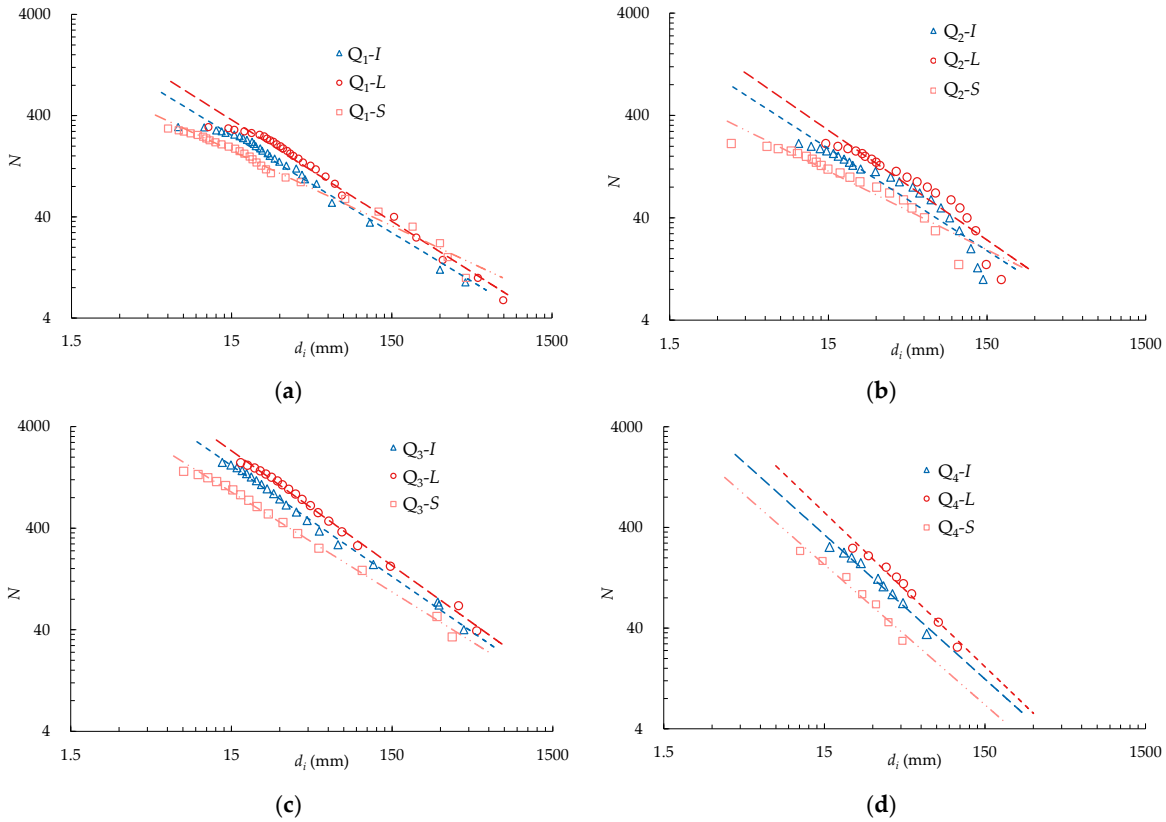


Figure 6. Power-law fractal distributions of blasting fragments obtained via the particle size–frequency method: (**a**) quarry Q_1; (**b**) quarry Q_2; (**c**) quarry Q_3; (**d**) quarry Q_4.

Table 3. Fitting results for the power-law fractal distribution of blasting fragments based on the particle size–frequency method.

Quarry Location	*L*			*I*			*S*		
	D	N_0	R^2	***D***	N_0	R^2	***D***	N_0	R^2
Q_1	1.03	9176.3	0.99	1.00	4074.2	0.99	0.74	1340.5	0.98
Q_2	1.12	6296.7	0.91	1.03	3252.4	0.91	0.83	1142.3	0.94
Q_3	1.09	41,866	0.98	1.05	25,638	0.98	1.99	13,112	0.99
Q_4	1.23	35,819	0.97	1.44	16,557	0.97	1.39	7470.3	0.97

3.3. Calculation of Fractal Dimensions of Blasting Fragmentation

The size–cumulative mass fractal distribution curves for each experiment were obtained using Equation (10), as shown in Figure 7. The fractal dimensions of fragmentation and the statistical scale-free intervals are presented in Tables 4 and 5, respectively.

As shown in Tables 4 and 5, R^2 for the particle size–cumulative mass was greater than 0.88 for all the blasting experiments conducted at the four quarries. In general, a coefficient of determination (R^2) above 0.8 indicates a good fitting effect. In most cases, the coefficient of determination (R^2) of the particle size fractal curve was always greater than 0.839 [43]. This indicates that the blasting fragmentation distribution had distinct fractal characteristics. Comparative fitting was performed, and the blasting fragmentation distribution fractal curves of experiments #1–#7, #11–#13, and #17 could be linearly fitted with two line segments in the bilogarithmic plane, i.e., the blasting fragments obtained from experiments #1–#7, #11–#13, and #17 exhibited two scale-free intervals. Thus, the blasting fragments obtained from these experiments exhibited self-similarity within two scale-free intervals, indicating dual fractal characteristics.

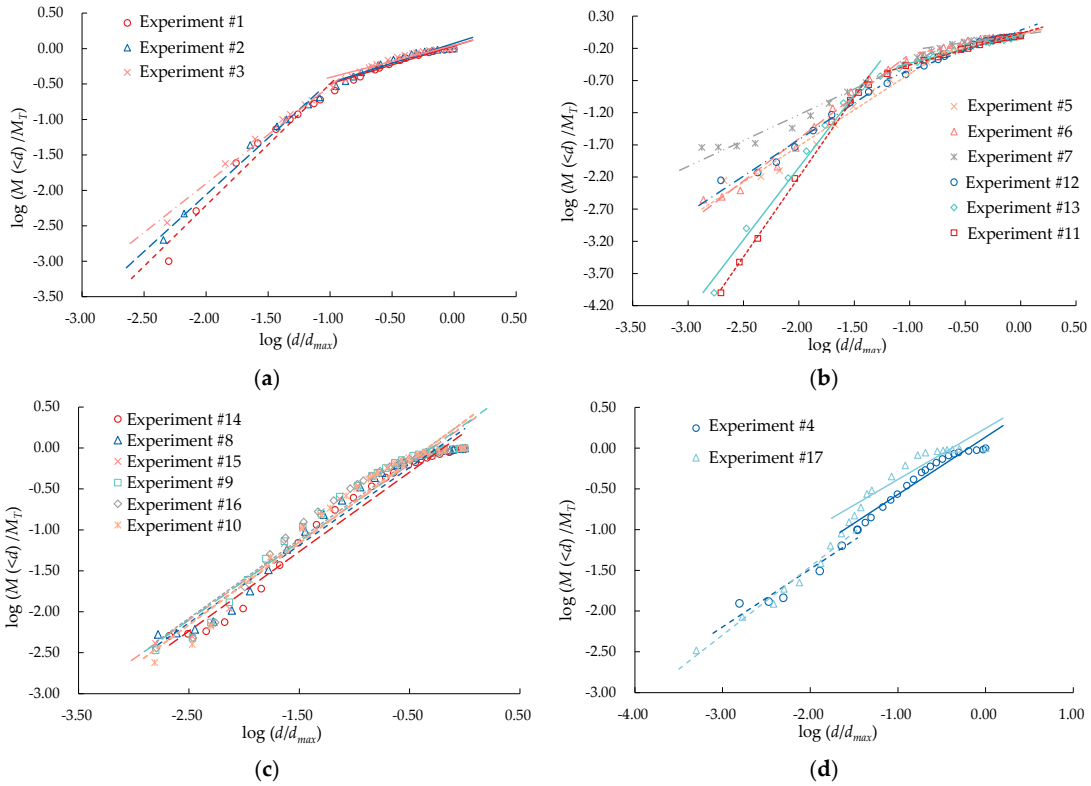


Figure 7. Relationship between the particle size and cumulative mass of blasting fragments in different quarries: (**a**) quarry Q_1 (experiments #1–#3); (**b**) quarry Q_3 (experiments #5–#7 and #11–#13); (**c**) quarry Q_3 (experiments #8–#10 and #14–#16); (**d**) quarries Q_2 (experiment #4) and Q_4 (experiment #17).

On the basis of Figure 7 and Tables 4 and 5, the fractal dimensions of blasting fragmentation (D_F) for each experiment are presented in Figure 8. As indicated by Tables 4 and 5 and Figure 8, influenced by factors such as physical and mechanical properties of the rock mass, joint distribution, excavation method, and blasting parameters, the scale-free intervals and D_F values differed significantly among the experiments, revealing multiple fractal characteristics. As shown in Figure 8a, the D_F differences were substantial between the two scale-free intervals, with D_F values mostly exceeding 2.3 in the large scale-free interval and remaining below 2.3—mostly below 2.0—in the small scale-free interval. This variation pattern is consistent with the multifractal characteristics variation observed by Sammis et al. [44] in the fault-gouge fragmentation process.

Table 4. Fractal dimensions of blasting fragments with dual fractal characteristics.

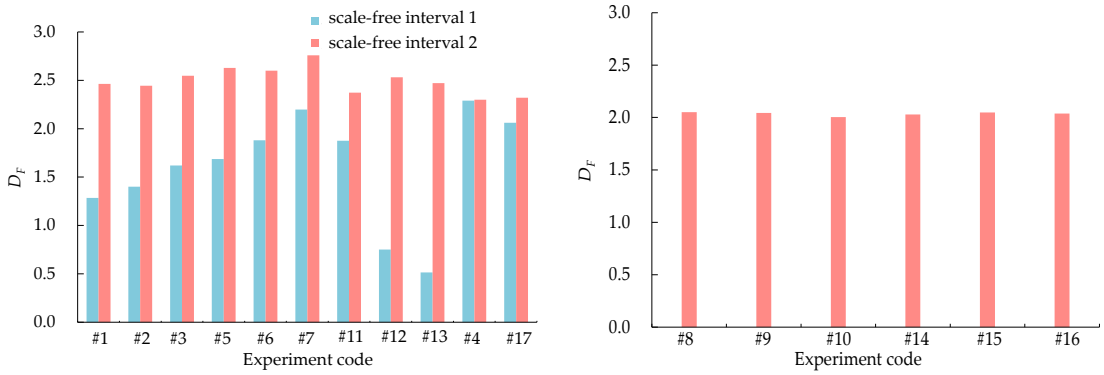
Quarry Location	Lithology	Experiment Code	Scale-Free Interval (mm)	Slope	R^2	D_F
Q_1	Limestone	#1	6–131	1.72	0.97	1.28
			131–1100	0.54	0.97	2.46
		#2	6.8–123	1.60	0.99	1.40
			123–1400	0.56	0.94	2.44
		#3	6.8–186	1.38	0.99	1.62
			186–1400	0.45	0.94	2.55
Q_2	Tuff	#4	3.2–70.1	0.71	0.94	2.19
			70.1–2030	0.71	0.91	2.30

Table 4. *Cont.*

Quarry Location	Lithology	Experiment Code	Scale-Free Interval (mm)	Slope	R^2	D_F
Q_3	Granite	#5	3.2–215	1.31	0.98	1.69
			215–2400	0.37	0.94	2.63
		#6	3.3–389	0.80	0.98	2.20
			389–2480	0.24	0.92	2.76
		#7	3.2–310	1.12	0.98	1.88
			310–1500	0.40	0.97	2.60
		#11	3.2–68	2.49	0.99	0.51
			68–1600	0.53	0.98	2.47
		#12	3.2–68	1.12	0.97	1.88
			68–1600	0.63	0.96	2.37
		#13	3.2–100	2.25	0.98	0.75
			100–1840	0.47	0.98	2.53
Q_4	Limestone	#17	3.35–55.2	0.94	0.97	2.06
			55.2–1988	0.68	0.88	2.32

Table 5. Fractal dimensions of blasting fragments with single fractal characteristics.

Quarry Location	Lithology	Experiment Code	Scale-Free Interval (mm)	Slope	R^2	D_F
Q_3	Granite	#8	3.2–1900	0.95	0.97	2.05
		#9	6.8–2030	0.96	0.96	2.04
		#10	3.1–2080	1.00	0.95	2.00
		#14	3.2–1500	0.97	0.97	2.03
		#15	3.5–2000	0.95	0.96	2.05
		#16	6.8–1970	0.96	0.96	2.04



(**a**) (**b**)

Figure 8. Fractal dimensions of blasting fragmentation in each experiment: (**a**) fractal dimensions of blasting experiments with dual fractal characteristics; (**b**) fractal dimensions of blasting experiments with single fractal characteristics.

The lithology of both quarries Q_1 and Q_4 is limestone. However, quarry Q_4 had a lower rock compressive strength, and experiment #17 employed a coupled explosive charging structure using mixed-porous granular ammonium nitrate. Under the action of blast loads, quarry Q_4 consumed more explosive energy near the boreholes, resulting in more pronounced fragmentation, which caused the small scale-free interval in experiment #17 to be narrower than those in experiments #1–#3. However, within the small scale-free interval, the D_F value in experiment #17 exceeded those in experiments #1–#3, indicating a higher level of fragmentation. Moreover, as shown in Figure 8a, despite significant differences in the large scale-free intervals between the two quarries, the variation in D_F remained minor.

The lithology of quarry Q_3 is granite. When the bench height was 12 m (experiments #5–#7 and #11–#13), the rock fragmentation exhibited multifractal characteristics. However,

when the bench height was 8 m (experiments #8–#10 and #14–#16), multifractal characteristics were not observed during the fragmentation process. When the bench height was 12 m, experiments #5–#7 and #11 employed blasting techniques involving shock-reflection devices and water-decked devices, respectively. These two excavation methods increased the transmission and reflection of stress waves within the rock, enhancing the fragmentation in the small scale-free interval and resulting in higher fragmentation levels and larger D_F values within the small scale-free interval than within the large interval. In addition, Figure 8b shows that when the bench height was 8 m, the blasting with shock-reflection devices (experiments #8–#10) and the conventional bench blasting technique (experiments #14–#16) yielded similar D_F values. However, the granite in this area had significant weathering; thus, further research into the effects of excavation methods on rock fragmentation characteristics is needed.

3.4. Calculation of Probability of Blasting Fragmentation

The fragmentation fractal dimension is a crucial parameter for studying the degree of rock fragmentation and fracture patterns. Because rock fragmentation exhibits self-similarity, Xie et al. [28] proposed the following formula for calculating the probability of rock fragmentation:

$$D_F = \frac{\log(nP_c)}{\log\left(\frac{1}{r}\right)}, \tag{11}$$

where P_c represents the probability of further rock fragmentation, r represents the fragmentation similarity ratio, and n represents the number of secondary fragmentation units.

At quarry Q_3, high-speed photography using the Phantom Veo710l camera was employed to monitor the granite-rock-blasting fragmentation process multiple times. The setup of the high-speed camera is illustrated in Figure 9. Through a comparative analysis of high-speed images of the bench surface before and after blasting, the macroscopic crack distribution on the bench surface was determined, as shown in Figure 10.

As shown in Figure 10, under the action of explosive energy, the rock of the bench surface underwent multistage fragmentation, with each stage resulting in smaller fragments of similar shape. According to fractal models such as the Sierpinski carpet, it can be learned from the macrocrack distribution in Figure 10 that the blasting fragmentation process of granite rock underwent two or three stages of fragmentation, with each stage involving a division into smaller fragments with similar shapes and a division factor of 2. This finding implies a fragmentation similarity ratio of 0.5, and the number of secondary fragmentation units was 8. Accordingly, the average blasting fragmentation probability for each experiment was calculated using Equation (11), and the results are shown in Figure 11.

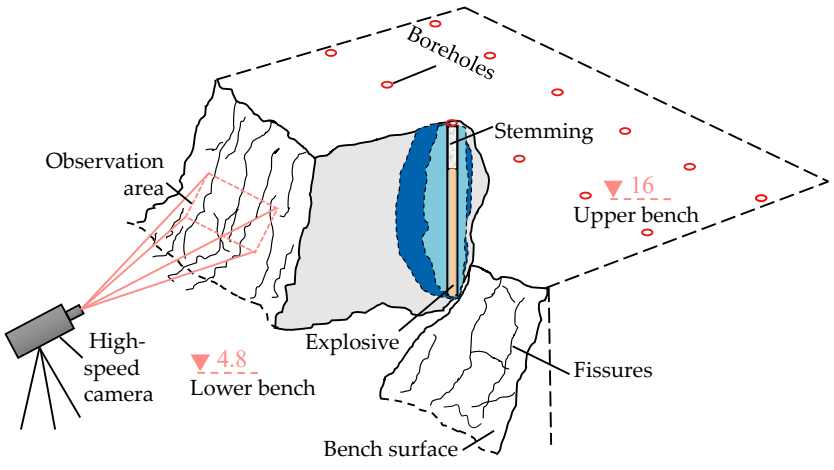
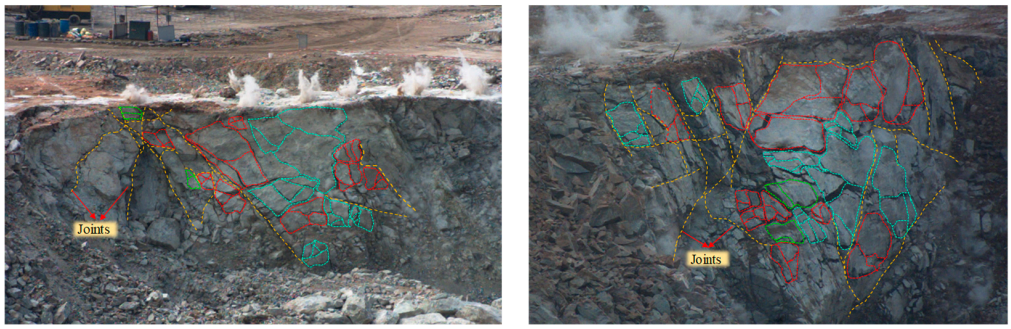


Figure 9. Schematic of high-speed photography monitoring of the rock fragmentation process in deep-hole bench blasting.



(**a**) (**b**)

Figure 10. High-speed photography images of the crack distribution of the bench surface during the blasting fragmentation of granite in quarry Q_3: (**a**) experiment #5; (**b**) experiment #11.

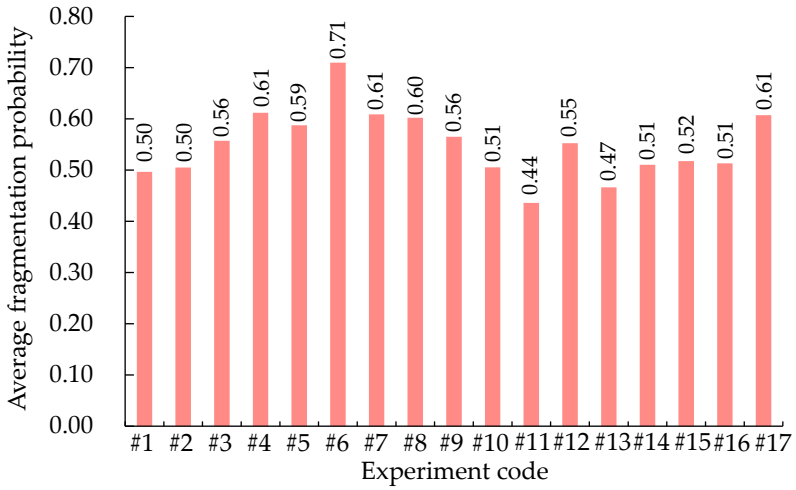


Figure 11. Average blasting fragmentation probability in each blasting experiment.

As shown in Figure 11, the average blasting fragmentation probabilities for the four quarries ranged from 0.44 to 0.71. Quarry Q_3, which consisted of granite, was excavated using three different methods (experiments #5–#16), resulting in a wide fluctuation range of fragmentation probabilities. When the bench height was the same, employing shock-reflection devices (experiments #5–#10) increased the blasting fragmentation probability. Therefore, adding a shock-reflection device at the bottom of the boreholes enhances the stress wave transmission and reflection, improving the blasting fragmentation effects.

4. SSA and Fractal Dimensions

Studies indicated that the fracture surfaces of rock particles also exhibit fractal structures [28]. For rock particles, the surface area S_F is related to the particle size d and the surface fractal dimension D_s as follows:

$$S_F \propto d^{D_s}. \tag{12}$$

By applying the Griffith energy balance criterion, Nagahama [45] analyzed the variations in the potential energy release rate and fracture-specific energy during the rock-particle fragmentation process, proposing a relationship between the SSA of rock particles and their surface fractal dimension:

$$\mathrm{SSA} \propto d^{D_s-3}. \tag{13}$$

Drawing on the research of Nagahama [45], Suzuki-Kamata et al. [46] used the Walker–Lewis energy equation to derive the relationship between the surface fractal dimension D_s and the fractal dimension of the particle size distribution D:

$$D_s = \frac{D+3}{2}. \tag{14}$$

Substituting Equation (14) into Equation (13) yields

$$\text{SSA} \propto d^{\frac{D-3}{2}}. \tag{15}$$

Carpinteri et al. [47] presented the relationship between the SSA of the fragmented material and the fragmentation fractal dimension D_F:

$$\text{SSA} \propto d^{D_F-3}. \tag{16}$$

Using a cubic model, Xie [28] established the relationship between the SSA of rock particles and the particle size:

$$\text{SSA} \propto d^{D-3}. \tag{17}$$

The exponents in Equations (13) and (15)–(17) can be regarded as the SSA exponents of rock particles. Detailed measurements and values of D_s and SSA for the blasting fragments randomly collected from the four quarries are presented in references [3,40]. Using the mean particle size distribution fractal dimension D and fragmentation fractal dimension D_F reported in Sections 3.1 and 3.2, the SSA exponents of blasting fragments randomly collected from the four quarries were computed using Equations (13) and (15)–(17). The results are shown in Figure 12.

As shown in Figure 12, the SSA exponents calculated using the surface fractal dimension D_s, fragmentation fractal dimension D_F, and particle size distribution fractal dimension D differed from the measured values. The errors are presented in Figure 13.

As shown in Figure 13, the SSA exponents calculated using Equation (16) and the fragmentation fractal dimension D_F exhibited the smallest differences from the measured values. Additionally, the findings presented in Section 3.3 indicate that the fragmentation fractal dimension is closely related to the probability of blasting fragmentation, which is associated with the newly generated surface area during the fragmentation process. Hence, the SSA, fragmentation energy, and energy utilization efficiency calculated according to the fragmentation fractal dimension align more closely with practical observations.

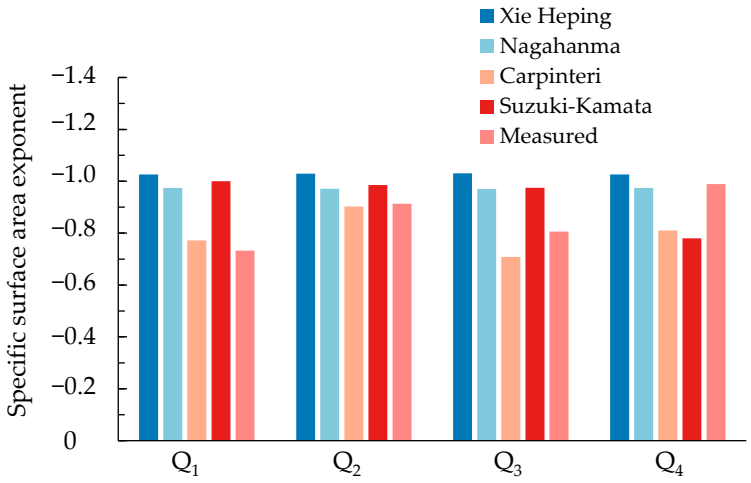


Figure 12. Comparison of SSA exponents.

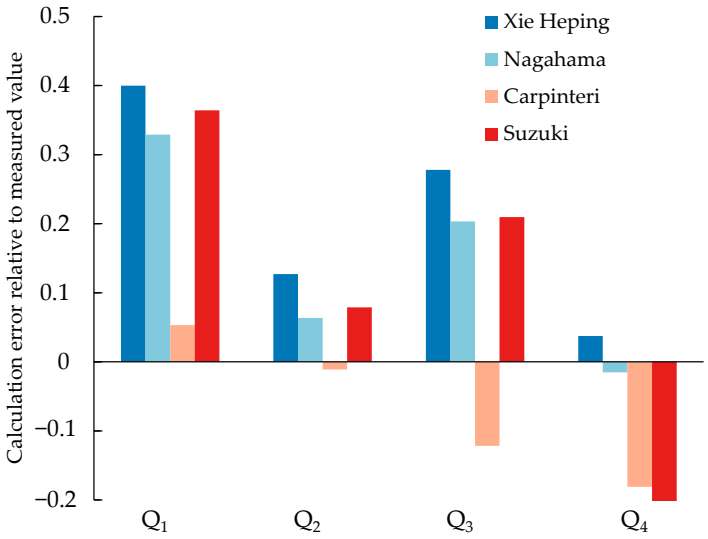


Figure 13. Comparison of the calculation errors for the SSA exponents.

According to the above analysis and the SSA presented in references [3,40], a predictive formula for calculating the SSA of blasting fragments using the fragmentation fractal dimension D_F and median particle size I is as follows:

$$\mathrm{SSA} = \lambda_1 I^{D_F-3} + \lambda_2, \tag{18}$$

where λ_1 and λ_2 are constants related to the lithology, rock fragmentation process, etc.

The SSAs of blasting fragments in the four quarries are presented in Figure 14. The figure indicates that both the fragmentation fractal dimension D_F and median particle size I yield R^2 values greater than 0.85 for the SSA, suggesting that the utilization of the fragmentation fractal dimension D_F and median particle size I provides accurate predictions of the SSA of blasting fragments. In subsequent research, the volumes and surface areas of blasting fragments with large particle sizes can be easily determined using 3D laser scanning technology, and λ_1 and λ_2 can be determined through fitting. Then, the SSAs of blasting fragments with a wide grading range can be calculated.

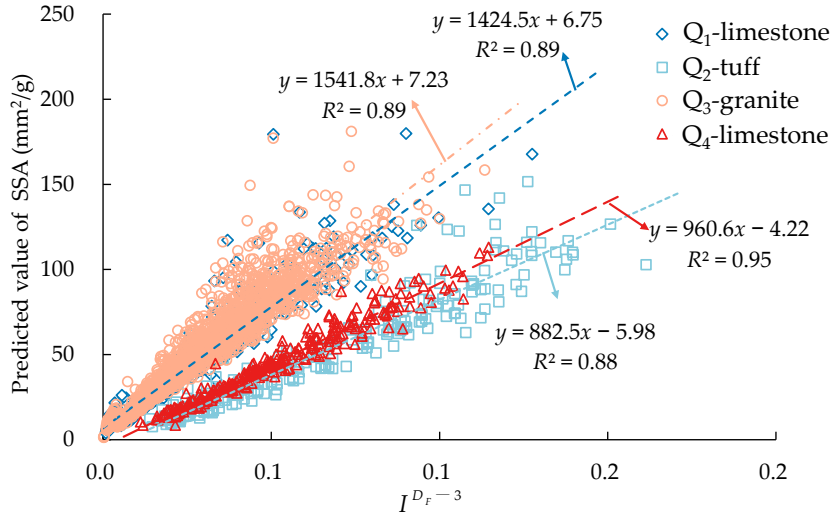


Figure 14. Predictive formulas for the SSAs of blasting fragments based on the fragmentation fractal dimension.

Because the fragmentation fractal dimension D_F is less than 3.0 and the SSA exponent is always less than 0, with a larger particle size, the SSA of blasting fragments is closer to the

origin. Therefore, as shown in Figure 14, the difference in SSA of blasting fragments with differences in lithology increases as the particle size decreases. According to the calculation results, the average D_F values of blasting fragments in the four quarries decrease in the order of Q_3, Q_1, Q_4, and Q_2. According to Figure 14, with a larger average D_F, the SSA increases faster with a reduction in particle size; thus, a larger D_F corresponds to a higher blasting fragmentation probability, more rock fragmentation, and a larger proportion of fragmentation energy in rock blasting. Moreover, all four quarries provide raw materials for downstream crushing processing. The further rock fragmentation due to blasting significantly reduces the energy consumption of downstream mechanical crushing.

Therefore, in the subsequent quarry blasting, the influence of the fragmentation fractal dimension D_F on the energy consumption of the mine-to-milling process can be further studied, and the blasting design can be optimized by establishing mathematical models to optimize the energy consumption of the whole process.

5. Conclusions

Through multiple field blasting experiments and indoor measurements of shape parameters of selected blasting fragments, the fractal characteristics of rock blasting fragments were investigated. The probability of rock blasting fragmentation was determined using the fragmentation fractal dimension, and a predictive formula for the SSA of blasting fragments was established. The following conclusions were drawn:

(1) According to the particle size–frequency relationship, the fractal dimensions of the particle size distribution calculated using different characteristic sizes were all less than 2, and the characteristic size significantly affected the computed fractal dimensions of the particle size distribution.

(2) Depending on the excavation methods, blasting parameters, and other factors, blasting experiments with multifractal characteristics exhibited significant variations in the scale-free intervals and fragmentation fractal dimensions. In the larger scale-free interval, the fragmentation fractal dimensions were mostly greater than 2.3, whereas in the smaller scale-free interval, they were often less than 2.0.

(3) Rock blasting fragmentation mainly involved two or three stages of fragmentation, with a similarity ratio of 0.5. The calculated average fragmentation probabilities of rock blasting ranged from 0.44 to 0.71. At the same bench height, blasting fragmentation with shock-reflection devices strengthened the transmission and reflective effects of stress waves, increasing the fragmentation probability and fragmentation efficiency of the rock mass.

(4) The SSA of blasting fragments was closely related to the fragmentation fractal dimension and median particle size. By determining the SSA of blasting fragments with large particle sizes using 3D laser scanning technology in advance, the SSA of blasting fragments with a wide grading range can be easily calculated via the SSA predictive formula.

Author Contributions: Conceptualization, R.L., S.L. and W.L.; methodology, R.L., Y.L. and P.Z.; software, C.D.; validation, S.L., Y.L. and W.L.; formal analysis, C.D.; investigation, P.Z., C.D. and Y.L.; resources, S.L., P.Z. and W.L.; data curation, C.D. and Y.L.; writing—original draft preparation, R.L. and P.Z.; writing—review and editing, R.L., Y.L. and P.Z.; visualization, C.D. and Y.L.; supervision, S.L., Y.L. and W.L.; project administration, P.Z. and S.L.; funding acquisition, R.L. All authors have read and agreed to the published version of the manuscript.

Funding: This research was funded by the Open Research Fund Project of Key Laboratory of Geotechnical Mechanics and Engineering of the Ministry of Water Resources, Yangtze River Scientific Research Institute (Grant No. CKWV20221012/KY), and the Major Science and Technology Program (201 Program) of PowerChina Huadong Engineering Corporation Limited (Grant No. KY2021-ZD-01).

Institutional Review Board Statement: Not applicable.

Informed Consent Statement: Not applicable.

Data Availability Statement: The data that support the findings of this study are available from the corresponding author upon reasonable request.

Acknowledgments: This work was completed with the contributions of many researchers and their achievements, to whom the authors express gratitude. To avoid omissions, we express thanks to all contributors.

Conflicts of Interest: Authors Ruize Li, Peng Zhu, Cong Ding and Yijia Liu were employed by the company Zhejiang Huadong Engineering Construction Management Company. The remaining authors declare that the research was conducted in the absence of any commercial or financial relationships that could be construed as a potential conflict of interest.

References

1. Shim, H.J.; Ryu, D.W.; Chung, S.K.; Syn, J.H.; Song, J.J. Optimized blasting design for large-scale quarrying based on a 3-D spatial distribution of rock factor. *Int. J. Rock Mech. Min. Sci.* **2009**, *46*, 326–332. [CrossRef]
2. Faramarzi, F.; Mansouri, H.; Farsangi, M.A.E. A rock engineering systems based model to predict rock fragmentation by blasting. *Int. J. Rock Mech. Min. Sci.* **2013**, *60*, 82–94. [CrossRef]
3. Li, R.Z.; Lu, W.B.; Chen, M.; Wang, G.H.; Xia, W.J.; Yan, P. Quantitative analysis of shapes and specific surface area of blasted fragments using image analysis and three-dimensional laser scanning. *Int. J. Rock Mech. Min. Sci.* **2021**, *141*, 104710. [CrossRef]
4. Ouchterlony, F. *Influence of Blasting on the Size Distribution and Properties of Muckpile Fragments, a State-of-the Art Review: MinFo Project P2000-10: Energy Optimisation during Comminution*; Swedish Mineral Research Organisation: Stockholm, Sweden, 2003.
5. De Cola, F. Mechanical Characterisation and Modelling of Statistically Representative Granular Materials Subjected to Impact Loading. Ph.D. Thesis, University of Oxford, Oxford, UK, 2017.
6. Taylor, M.A. Quantitative measures for shape and size of particles. *Powder Technol.* **2002**, *124*, 94–100. [CrossRef]
7. Ouchterlony, F.; Sanchidrián, J.A. A review of development of better prediction equations for blast fragmentation. *J. Rock Mech. Geotech. Eng.* **2019**, *11*, 1094–1109. [CrossRef]
8. Wills, B.A.; Finch, J.A. *Wills' Mineral Processing Technology*, 8th ed.; Butterworth-Heinemann: Oxford, UK, 2015.
9. Snowsill, W.L. Particle sizing. In *Instrumentation Reference Book*, 4th ed.; Boyes, W., Ed.; Butterworth-Heinemann: Oxford, UK, 2003; pp. 175–189.
10. Asl, P.F.; Monjezi, M.; Hamidi, J.K.; Armaghani, D.J. Optimization of flyrock and rock fragmentation in the Tajareh limestone mine using metaheuristics method of firefly algorithm. *Eng. Comput.* **2018**, *34*, 241–251. [CrossRef]
11. Dimitraki, L.; Christaras, B.; Marinos, V.; Vlahavas, I.; Arampelos, N. Predicting the average size of blasted rocks in aggregate quarries using artificial neural networks. *Bull. Eng. Geol. Environ.* **2019**, *78*, 2717–2729. [CrossRef]
12. Babaeian, M.; Ataei, M.; Sereshki, F.; Sotoudeh, F.; Mohammadi, S. A new framework for evaluation of rock fragmentation in open pit mines. *J. Rock Mech. Geotech. Eng.* **2019**, *11*, 325–336. [CrossRef]
13. Onederra, I.; Thurley, M.J.; Catalan, A. Measuring blast fragmentation at Esperanza mine using high-resolution 3D laser scanning. *Min. Technol.* **2015**, *124*, 34–36. [CrossRef]
14. Chen, N.; Kemeny, J.; Jiang, Q.H.; Pan, Z.W. Automatic extraction of blocks from 3D point clouds of fractured rock. *Comput. Geosci.* **2017**, *109*, 149–161. [CrossRef]
15. Campbell, A.D.; Thurley, M.J. Application of laser scanning to measure fragmentation in underground mines. *Min. Technol.* **2017**, *126*, 240–247. [CrossRef]
16. Masad, E.; Saadeh, S.; Al-Rousan, T.; Garboczi, E.; Little, D. Computations of particle surface characteristics using optical and X-ray CT images. *Comput. Mater. Sci.* **2005**, *34*, 406–424. [CrossRef]
17. Al Rousan, T.M. Characterization of Aggregate Shape Properties Using a Computer Automated System. Doctoral Dissertation, Texas A&M University, College Station, TX, USA, 2005.
18. Masad, E.; Button, J.W. Unified imaging approach for measuring aggregate angularity and texture. *Comput.-Aided Civ. Infrastruct. Eng.* **2000**, *15*, 273–280. [CrossRef]
19. Liu, Y.F.; Sun, W.J.; Nair, H.; Lane, D.S.; Wang, L.B. Quantification of aggregate morphologic characteristics with the correlation to uncompacted void content of coarse aggregates in Virginia. *Constr. Build. Mater.* **2016**, *124*, 645–655. [CrossRef]
20. Hryciw, R.D.; Zheng, J.; Shetler, K. Particle roundness and sphericity from images of assemblies by chart estimates and computer methods. *J. Geotech. Geoenviron. Eng.* **2016**, *142*, 04016038. [CrossRef]
21. Blott, S.J.; Pye, K. Particle shape: A review and new methods of characterization and classification. *Sedimentology* **2008**, *55*, 31–63. [CrossRef]
22. Tunwal, M.; Mulchrone, K.F.; Meere, P.A. Quantitative characterization of grain shape: Implications for textural maturity analysis and discrimination between depositional environments. *Sedimentology* **2018**, *65*, 1761–1776. [CrossRef]
23. Zhu, H.J.; Fang, H.Y.; Cai, Y.Y.; Lv, N. Development of a rapid measurement system for coarse aggregate morphological parameters. *Particuology* **2020**, *50*, 181–188. [CrossRef]
24. Barrett, P.J. The shape of rock particles, a critical review. *Sedimentology* **1980**, *27*, 291–303. [CrossRef]
25. Tromans, D.; Meech, J.A. Fracture toughness and surface energies of minerals: Theoretical estimates for oxides, sulphides, silicates and halides. *Miner. Eng.* **2002**, *15*, 1027–1041. [CrossRef]

26. Ouhbi, N.; Voivret, C.; Perrin, G.; Roux, J.-N. 3D particle shape modelling and optimization through proper orthogonal decomposition. *Granul. Matter* **2017**, *19*, 86. [CrossRef]
27. Hyslip, J.P.; Vallejo, L.E. Fractal analysis of the roughness and size distribution of granular materials. *Eng. Geol.* **1997**, *48*, 231–244. [CrossRef]
28. Xie, H.P. *Introduction to Fractals and Rock Mechanics*; China Science Publishing & Media Ltd. (CPSM): Beijing, China, 1996.
29. Su, D.; Wang, X.; Yang, H.W.; Hong, C.Y. Roughness analysis of general-shape particles, from 2D closed outlines to 3D closed surfaces. *Powder Technol.* **2019**, *356*, 423–438. [CrossRef]
30. Guo, Y.L.; Markine, V.; Zhang, X.H.; Qiang, W.L.; Jing, G.Q. Image analysis for morphology, rheology and degradation study of railway ballast: A review. *Transp. Geotech.* **2019**, *18*, 173–211. [CrossRef]
31. Li, J.; Liu, C.; Liu, H.M.; Wang, J.D.; Zeng, Z.P.; Xie, Y.T. Study on meso-damage damage mechanism of shale reservoir rock based on digital core. *Chin. J. Rock Mech. Eng.* **2022**, *41*, 1103–1113.
32. Wang, L.; Yuan, Q.P.; Xie, G.X.; Gu, S.H.; Jiao, Z.H.; Liu, H.Q.; Chen, L.P. Length-diameter ratio effect of energy dissipation and fractals of coal samples under impact loading. *J. China Coal Soc.* **2022**, *47*, 1534–1546.
33. Luo, H.H.; Yang, R.S.; Ma, X.M.; Yang, G.L.; Zhu, P.X.; Feng, W.Y. Study on distribution characteristics of deep hole in the fan-shaped hole of Shilu Iron Mine. *J. Min. Saf. Eng.* **2023**, *40*, 371–378.
34. Sun, Q.; Duan, F.B.; Xie, H.P. Study on fractal dimension evaluation measurement of coal rock blasting. *Chin. J. Rock Mech. Eng.* **2000**, *19*, 505–508.
35. Ouchterlony, F.; Nyberg, U.; Olsson, M.; Bergqvist, I.; Granlund, L.; Grind, H. Where does the explosive energy in rock blasting rounds go? *Sci. Technol. Energetic Mater.* **2004**, *65*, 54–63.
36. Hamdi, E.; Romdhane, N.B.; du Mouza, J.; Le Cleac'h, J.M. Fragmentation energy in rock blasting. *Geotech. Geol. Eng.* **2008**, *26*, 133–146. [CrossRef]
37. Jiang, S.; Shen, L.M.; Guillard, F.; Einav, I. Energy dissipation from two-glass-bead chains under impact. *Int. J. Impact Eng.* **2018**, *114*, 160–168. [CrossRef]
38. Merkus, H.G. Sieves and sieving. In *Particle Size Measurements*; Particle Technology Series; Springer: Dordrecht, The Netherlands, 2009; Volume 17, pp. 219–240.
39. Singh, P.K.; Roy, M.P.; Paswan, R.K.; Sarim, M.; Kumar, S.; Jha, R.R. Rock fragmentation control in opencast blasting. *J. Rock Mech. Geotech. Eng.* **2016**, *8*, 225–237. [CrossRef]
40. Li, R.Z.; Lu, W.B.; Yin, Y.J.; Yu, Y.J.; Chen, M.; Xia, W.J.; Yan, P. Study on the shape and specific surface area characteristics of blasting gravel particles of limestone in Hangudi quarry of Baihetan. *Chin. J. Rock Mech. Eng.* **2019**, *38*, 1344–1354.
41. Wu, Y.; Ma, G.; Zhou, W.; Yang, L.F. Optimization of gradation of rockfill materials based on the fractal theory. *Rock Soil Mech.* **2016**, *37*, 1977–1985.
42. Li, D.J.; Jia, X.N.; Miao, J.L.; He, M.C.; Li, D.D. Analysis of fractal characteristics of fragment from rockburst test of granite. *Chin. J. Rock Mech. Eng.* **2010**, *29*, 3280–3289.
43. Tyler, S.W.; Wheatcraft, S.W. Fractal scaling of soil particle-size distributions: Analysis and limitations. *Soil Sci. Soc. Am. J.* **1992**, *56*, 362–369. [CrossRef]
44. Sammis, C.G.; Biegel, R.L. Fractals, fault-gouge, and friction. *Pure Appl. Geophys.* **1989**, *131*, 255–271. [CrossRef]
45. Nagahama, H. Fractal scalings of rock fragmentation. *Earth Sci. Front.* **2000**, *7*, 169–177.
46. Suzuki-Kamata, K.; Kusano, T.; Yamasaki, K. Fractal analysis of the fracture strength of lava dome material based on the grain size distribution of block-and-ash flow deposits at Unzen Volcano, Japan. *Sediment. Geol.* **2009**, *220*, 162–168. [CrossRef]
47. Carpinteri, A.; Lacidogna, G.; Pugno, N. Scaling of energy dissipation in crushing and fragmentation: A fractal and statistical analysis based on particle size distribution. *Int. J. Fract.* **2004**, *129*, 131–139. [CrossRef]

Disclaimer/Publisher's Note: The statements, opinions and data contained in all publications are solely those of the individual author(s) and contributor(s) and not of MDPI and/or the editor(s). MDPI and/or the editor(s) disclaim responsibility for any injury to people or property resulting from any ideas, methods, instructions or products referred to in the content.